catalysts

MDPI

Supplementary Materials

In Situ Growth of Exsolved Nanoparticles under Varying rWGS Reaction Conditions—A Catalysis and Near Ambient Pres-sure-XPS Study

Lorenz Lindenthal [1,†], Joel Huber [1,†], Hedda Drexler [1], Thomas Ruh [1], Raffael Rameshan [1], Florian Schrenk [1], Stefan Löffler [2] and Christoph Rameshan [1,*]

[1] Institute of Materials Chemistry, TU Wien, Getreidemarkt 9/165-PC, 1060 Vienna, Austria; lorenz.lindenthal@tuwien.ac.at (L.L.); e1425216@student.tuwien.ac.at (J.H.); hedda.drexler@tuwien.ac.at (H.D.); thomas.ruh@tuwien.ac.at (T.R.); raffael.rameshan@tuwien.ac.at (R.R.); florian.schrenk@tuwien.ac.at (F.S.)

[2] USTEM, TU Wien, Wiedner Hauptstr. 8-10/EO57-02, 1040 Vienna, Austria; stefan.loeffler@tuwien.ac.at (S.L.)

* Correspondence: christoph.rameshan@tuwien.ac.at (C.R.); Tel.: +43-1-58801-165115

† Co-first authors

Citation: Lindenthal, L.; Huber, J.; Drexler, H.; Ruh, T.; Rameshan, R.; Schrenk, F.; Löffler, S.; Rameshan, C. In Situ Growth of Exsolved Nanoparticles under Varying rWGS Reaction Conditions—A Catalysis and Near Ambient Pressure-XPS Study. *Catalysts* **2021**, *11*, 1484. https://doi.org/10.3390/catal11121484

Academic Editor: Alain Roucoux

Received: 10 November 2021
Accepted: 2 December 2021
Published: 3 December 2021

Publisher's Note: MDPI stays neutral with regard to jurisdictional claims in published maps and institutional affiliations.

1. Scanning Electron Microscopy (SEM) and particle analysis

For valid interpretation of the SEM data, several images of different positions were recorded and analysed for each sample. In the main paper, only selected images are shown; here, the full series of images are given for completeness. The results differ slightly between various sample positions, but the discussed general trends are still justified taking all images into account.

Figure S1 shows images obtained on $Nd_{0.6}Ca_{0.4}Fe_{0.9}Co_{0.1}O_{3-\delta}$ after the catalytic ramp experiments up to 700 °C, using different reverse Water-Gas Shift (rWGS) reaction atmospheres (CO_2 to H_2 1:1, 10:1, and 15:1). Additionally, histograms depict the associated determined particle size distributions. Table S1 gives further details regarding the particle analyses, as well as several statistical measures characterising the particle distributions.

Sample replicates under the same conditions revealed similar trends, despite independent analysis. Mostly right-skewed distributions were found, resembling log-normal distributions. The exception was Image (a) in case of the 10:1 ratio. However, this was the image where the lowest amounts of particles were included in the analysis, as it was difficult to find suitable sampling areas for particle analysis (homogeneous brightness in the cut-out region). Thus, the statistical error is largest for this image.

Mean particle diameters d_p increased, while numbers of particles per area decreased for the 1:1 gas ratio (mean d_p between 32.5 nm and 43.0 nm, between 29 and 47 particles per μm²) compared to the 15:1 gas ratio (mean d_p between 28.7 and 29.9 nm, between 48 and 84 particles per μm²). This trend was discussed in the main paper, and the results for the 10:1 gas ratio (mean d_p between 27.7 nm and 39.0 nm, between 31 and 53 particles per μm²) match the trend. Furthermore, the variance is lower with a higher CO_2 partial pressure, which means a narrower distribution under these conditions.

Images of $Nd_{0.6}Ca_{0.4}Fe_{0.9}Co_{0.1}O_{3-\delta}$ after the double ramp experiments with an end temperature of 570 °C are displayed in Figure S2, the respective details and results of the particle analyses are given in Table S2. Compared to the results of the 1:1 gas ratio and going up to 700 °C (although without the cooling ramp), the particles are on average smaller (mean d_p between 12.9 nm and 16.5 nm, when few larger particles clearly being not a result of exsolution are excluded) and more densely distributed (36 to 94 particles per μm²), as discussed in the main paper.

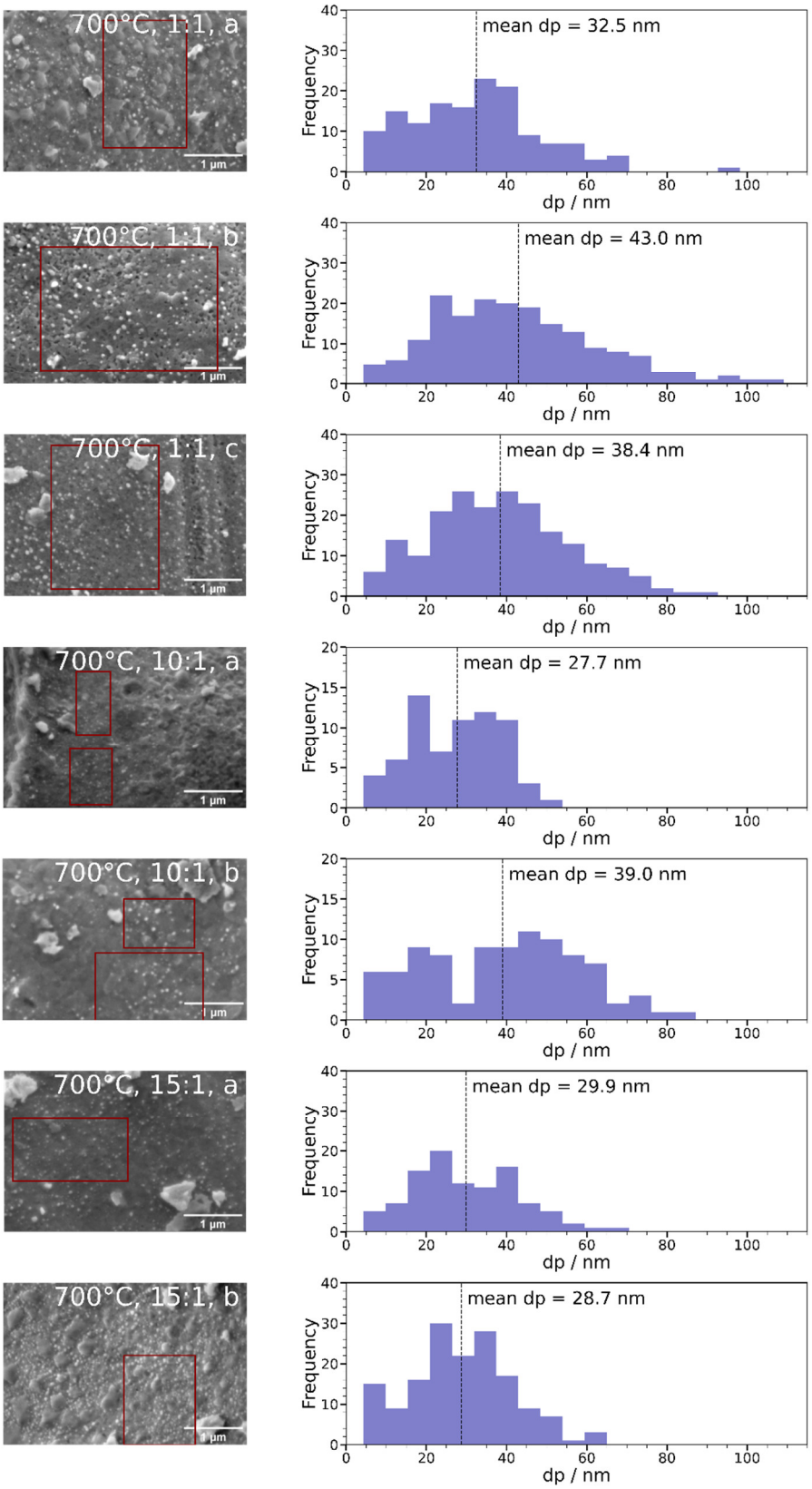

Figure S1. Left: SEM images of $Nd_{0.6}Ca_{0.4}Fe_{0.9}Co_{0.1}O_{3-\delta}$ after ramp experiments up to 700 °C with three different CO_2 to H_2 ratios of the reaction atmosphere. Different positions of the same samples are shown (for each sample consecutively denoted with letters). Right: Corresponding histograms of the sampled areas (red cut-outs) of the respective SEM image on the left. Additional details about the particle analyses and the determined particle distributions are given in Table S1.

Table S1. Parameter summary obtained from the particle analyses conducted on SEM images of $Nd_{0.6}Ca_{0.4}Fe_{0.9}Co_{0.1}O_{3-\delta}$ after rWGS with varying CO_2 to H_2 ratios, and statistical measures of the determined particle distributions. The respective images and histograms are displayed in Figure S1.

CO_2 : H_2 ratio	**1:1**	**1:1**	**1:1**	**10:1**	**10:1**	**15:1**	**15:1**
image	**a**	**b**	**c**	**a**	**b**	**a**	**b**
pixel area / nm²	7.38	7.30	7.30	7.23	7.07	7.27	7.34
sampled picture area / µm²	3.12	6.41	4.53	1.30	3.02	2.11	1.86
number of particles	145	185	201	69	93	102	157
particles per area / µm^{-2}	47	29	44	53	31	48	84
mean d_p / nm	32.5	43.0	38.4	27.7	39.0	29.9	28.7
variance / nm²	260	433	293	130	376	171	163
skewness	0.538	0.742	0.360	-0.0253	0.0094	0.383	0.228
kurtosis	0.572	0.587	-0.220	-0.931	-0.746	-0.172	-0.160

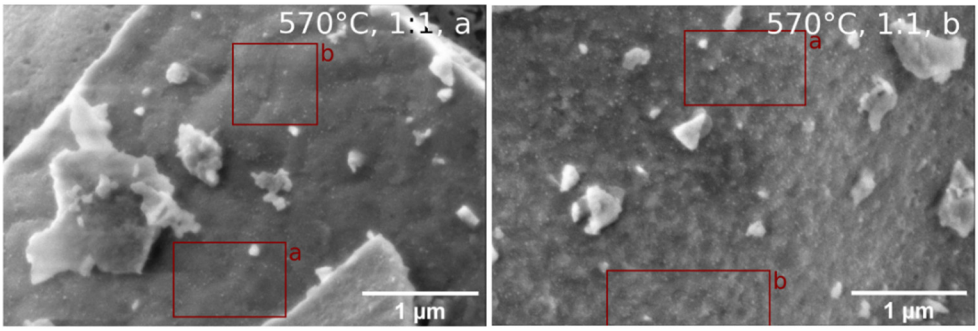

Figure S2. SEM images of $Nd_{0.6}Ca_{0.4}Fe_{0.9}Co_{0.1}O_{3-\delta}$ after double ramp catalytic tests with an end temperature of 570 °C. The two images (**a,b**) represent different positions of the same sample. The formation of finely dispersed nanoparticles on the surface was visible, but no formation of $CaCO_3$ crystallites could be observed. The cut-outs (marked red) were used for detailed particle analysis, results are shown in Table S2.

Table S2. Overview of the particle analysis for the sample $Nd_{0.6}Ca_{0.4}Fe_{0.9}Co_{0.1}O_{3-\delta}$ after double ramp experiments with end temperature 570 °C (respective images and cut-outs displayed in Figure S2). Larger particles were excluded from the calculation of the mean particle diameter d_p. The maximal included d_p is given, as well as the overall maximal found d_p (given in brackets) in the respective cut-out.

image	**a**		**b**	
cut-out	a	b	a	b
pixel area / nm²	7.27	7.27	7.19	7.19
sampled picture area / µm²	0.606	0.500	0.651	0.459
number of particles	22	24	61	25
particles per area / µm^{-2}	36	48	94	54
mean d_p / nm	15.6	12.9	13.3	16.5
d_p max. particle / nm	27.9 (120)	29.2	34.1 (87.6)	32.4 (73.6)

2. X-Ray Diffraction (XRD) Characterisation

2.1 Results and Discussion

To additionally thoroughly characterise the catalysts, XRD patterns of the three investigated materials were obtained both in the pristine state and after rWGS double ramp experiments (Figures S3–S5). The results corroborate the activating and deactivating effects discussed in the main paper. For all materials, the evolution of metallic species can be seen, leading to activation, as well as formation of $CaCO_3$, causing the deactivation.

In case of the Co-doped materials, the metallic species is a bcc phase, which indicates Fe as a main component (Co would have an fcc structure at this temperature). As metallic Co was observed with XPS, this is most likely an FeCo alloy. The 110 reflex of this species is centred at a 2θ value of 45.0° for $Nd_{0.6}Ca_{0.4}Fe_{0.9}Co_{0.1}O_{3-\delta}$ and at 44.8° for $Nd_{0.6}Ca_{0.4}Fe_{0.97}Co_{0.03}O_{3-\delta}$. This slight shift might be due to a higher Co content of the alloy in case of the material with 10 % Co-doping (Co is slightly smaller than Fe, a higher Co content thus means smaller lattice parameters and a shift to higher angles). For both materials, this 110 reflex is larger and narrower after the experiment with 700 °C end temperature. This supports the discussed ongoing exsolution at higher temperatures. Also, the narrower Bragg peak is a result of larger particles, in accordance with the different particle sizes observed with SEM.

Similarly, the 104 reflex of $CaCO_3$ is more prominent after going up to the higher temperature, agreeing with an increasing carbonate signal in this temperature range during the XPS experiments. The fact that both activating and deactivating phases continue to grow at high temperatures is responsible for the very different catalytic behaviour during the cooling phases of the ramp experiments with different maximum temperatures. A lower Co content in the exsolved metallic phase might be the reason why the activation effect cannot counteract the deactivation in case of only 3 % doping, as Fe is less active for rWGS than Co.

Interestingly, two discrepancies occur with respect to other experiments: (i) A metal phase is observed in XRD after going up to only 570 °C for the material with 10 % Co-doping; for the same material, in the XPS experiments no metallic states were observed up to 600 °C. (ii) In in situ XRD experiments with the same material, a $Co_{1-x}Fe_xO$ phase was observed during reaction [1], which is not seen in the ex situ measurements.

A possible explanation for both observations is that the $Co_{1-x}Fe_xO$ phase is only present under reaction conditions at elevated temperatures. Thus, during cooling, this phase, which formed at 570 °C, transformed to the metallic bcc phase which was detected with XRD. However, with XPS it is not distinguishable from lattice Fe and Co of the perovskite. Additionally, one has to keep in mind the different pressures used in the two experiments (1 bar for XRD and 1 mbar for XPS). Thus, Co might have been reduced already at a lower temperature at the higher pressure.

In case of $Nd_{0.6}Ca_{0.4}Fe_{0.97}Ni_{0.03}O_{3-\delta}$, two metallic species were found, again a bcc phase (110 reflex at a 2θ value of 44.8°) and a small amount of an fcc phase (202 reflex at a diffraction angle of 43.8°). The bcc structure corresponds to metallic Fe, fcc is the structure of Ni. Whether these phases are pure metals or alloys with the respective metal as a main component cannot be determined from the XRD pattern. However, this result is consistent with XPS findings, which showed evolution of metallic Ni at lower temperatures (the fcc phase), and formation of metallic Fe (the bcc phase) only at higher temperatures. Again, there is a discrepancy regarding the temperatures, the bcc phase was formed both at 600 °C and 700 °C, although metallic Fe could only be observed from 660 °C upwards with XPS. The above-mentioned pressure gap can explain this discrepancy.

Unlike with the Co-doped samples, the difference between the amounts of the evolved new phases between the two end temperatures is only minor in case of the Ni-doped material. Consequently, the catalytic behaviour during the two cooling ramps was very similar. The XRD results suggest that the material is relatively stable under reaction conditions in the temperature range between 600 °C and 700 °C.

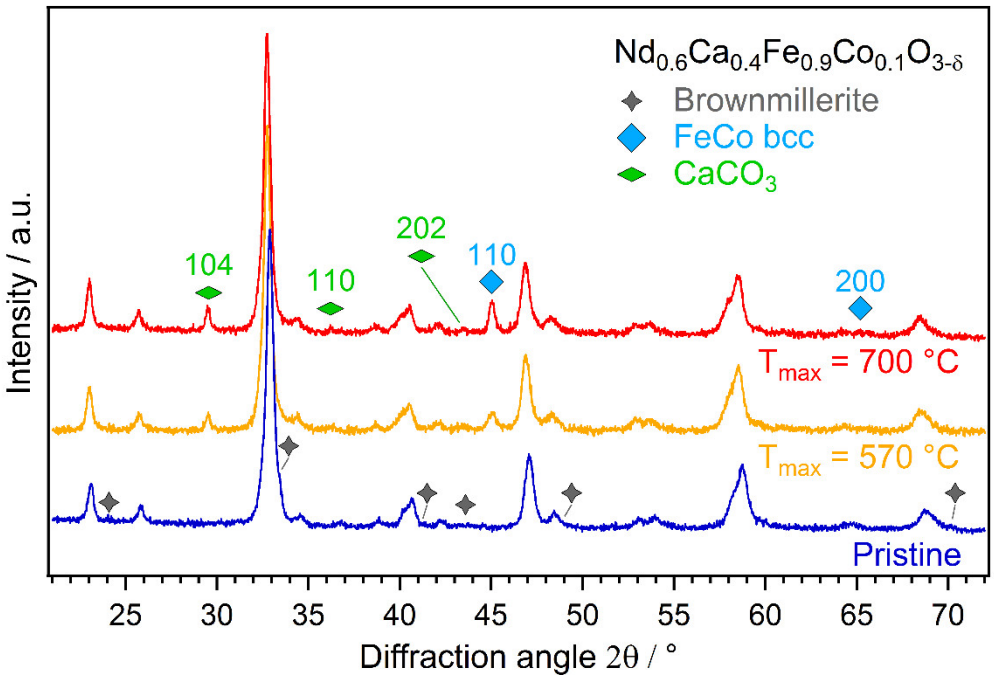

Figure S3. XRD pattern of $Nd_{0.6}Ca_{0.4}Fe_{0.9}Co_{0.1}O_{3-\delta}$ before (blue) and after the rWGS double ramp experiments (orange and red for ramp end temperatures of 570 °C and 700 °C, respectively). After both experiments, a metallic FeCo bcc phase and $CaCO_3$ were present, both more prominent in the experiment with a higher end temperature of 700 °C. Unlike in the samples with 3 % doping, there is only a very small contribution of a Brownmillerite phase (ordered oxygen vacancies) in the pristine sample, which vanishes after the experiment.

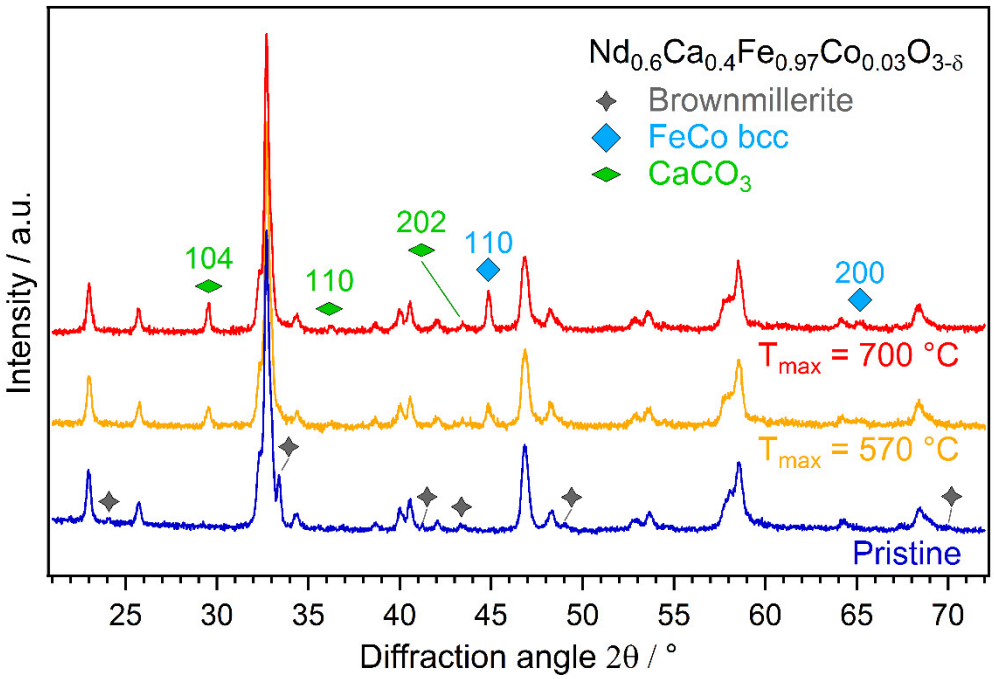

Figure S4. XRD pattern of $Nd_{0.6}Ca_{0.4}Fe_{0.97}Co_{0.03}O_{3-\delta}$ before (blue) and after the rWGS double ramp experiments (orange and red for ramp end temperatures of 570 °C and 700 °C, respectively). After both experiments, a metallic FeCo bcc phase and $CaCO_3$ were present, both more prominent in the experiment with a higher end temperature of 700 °C. A Brownmillerite phase (ordered oxygen vacancies) in the pristine sample vanishes after the experiment.

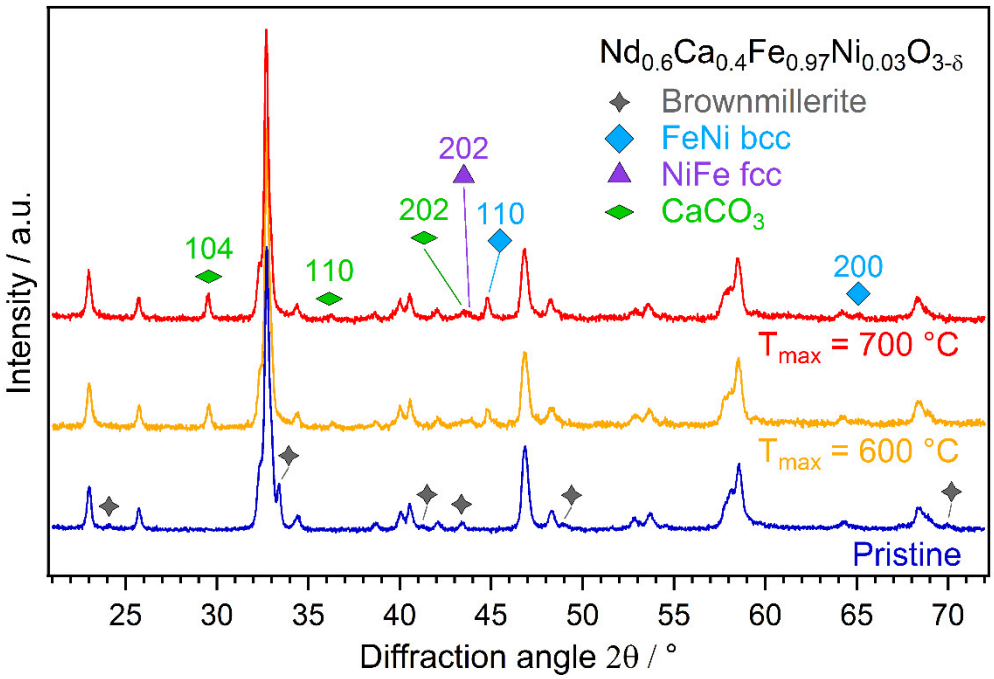

Figure S5. XRD pattern of $Nd_{0.6}Ca_{0.4}Fe_{0.97}Ni_{0.03}O_{3-\delta}$ before (blue) and after the rWGS double ramp experiments (orange and red for ramp end temperatures of 600 °C and 700 °C, respectively). After both experiments, two metallic FeNi phases formed, a bcc phase (main component Fe) and an fcc phase (main component Ni). $CaCO_3$ was present as well. A Brownmillerite phase (ordered oxygen vacancies) in the pristine sample vanishes after the experiment.

2.2. Experimental

A PANalytical X'Pert Pro diffractometer (Malvern Panalytical, Malvern, UK) in Bragg-Brentano geometry (with separated Cu $K_{\alpha 1,2}$ radiation) and an X'Celerator linear detector was used to perform XRD measurements. Data analysis and reflex assignment were performed with the HighScore Plus software (PANalytical) and the PDF-4+ 2021 database (ICDD - International Centre for Diffraction Data) [2].

Author Contributions: Conceptualisation, L.L., C.R. and T.R.; methodology, L.L, S.L. and C.R.; validation, L.L., R.R. H.D. and F.S.; formal analysis, L.L., R.R., H.D., F.S. and T.R.; investigation, J.H., L.L., S.L. and F.S.; resources, S.L. and C.R.; data curation, J.H., L.L., R.R., H.D. and T.R..; writing—original draft preparation, J.H. and L.L.; writing—review and editing, J.H., L.L., T.R. and C.R.; visualisation, J.H., L.L. and H.D.; supervision, C.R.; project administration, C.R.; funding acquisition, C.R. All authors have read and agreed to the published version of the manuscript.

Funding: This project has received funding from the European Research Council (ERC) under the European Union's Horizon 2020 research and innovation programme (grant agreement n° 755744 / ERC - Starting Grant TUCAS).

Data Availability Statement: The data presented in this study are available on request from the corresponding author.

Conflicts of Interest: The authors declare no conflict of interest.

References

1. Lindenthal, L.; Popovic, J.; Rameshan, R.; Huber, J.; Schrenk, F.; Ruh, T.; Nenning, A.; Löffler, S.; Opitz, A.K.; Rameshan, C. Novel perovskite catalysts for CO_2 utilization - Exsolution enhanced reverse water-gas shift activity. *Applied Catalysis B: Environmental* **2021**, *292*, 120183, doi:https://doi.org/10.1016/j.apcatb.2021.120183.
2. Gates-Rector, S.; Blanton, T. The Powder Diffraction File: a quality materials characterization database. *Powder Diffraction* **2019**, *34*, 352-360, doi:10.1017/S0885715619000812.